Effect of Al on Microstructure and Mechanical Properties of ATI 718Plus by Laser Additive Manufacturing

Zhipeng Zhang[1,2,3] · Jide Liu[3] · Xinguang Wang[3] · Zhaokuang Chu[3] · Yizhou Zhou[3] · Jianjun Wang[1,2] · Jinguo Li[3]

Abstract

To clarify the mechanism of the role of Al element in the additive manufacturing of Ni-based superalloys, ATI 718Plus alloys with varying Al contents (1, 3, and 5 wt%) were fabricated using the laser additive manufacturing and the effects of Al content on the microstructure and mechanical properties were systematically analyzed. The experimental and CALPHAD simulation results show that with the increase in Al addition, the freezing range of the alloys was lowered, but this has a paradoxical effect on the susceptibility of the alloy to hot-tearing and solid-state cracking. The addition of Al increased the γ' and Laves phase volume fractions and suppressed the precipitation of the η phase. Simultaneously improving γ/γ' lattice misfits effectively promoted the transformation of γ' phase from spherical to cubic. The precipitation of NiAl phase in the 5 wt% Al-added alloy was determined, the formation mechanism of NiAl phase was analyzed, and the solidification sequence of the precipitated phase in the alloy was summarized. In addition, with the increase in Al addition, the microhardness of the alloy increased gradually, the tensile strength increased at first and then decreased, but the plasticity deteriorated seriously. The insights gained from this study offer valuable theoretical guidance for the strategic compositional design of additively manufactured Ni-based superalloys destined for deployment under extreme conditions.

Keywords Laser additive manufacturing · ATI 718Plus · Laves phase · Microstructure · Mechanical properties

1 Introduction

Laser additive manufacturing (LAM) represents a cutting-edge technology for the rapid, free-form fabrication of three-dimensional solids from powder, enabling the creation of intricate structural components that pose challenges to conventional manufacturing techniques [1, 2]. Laser metal deposition (LMD) is one of the typical metal powder LMA systems, with high raw material utilization efficiency, saving product development cycles and processing costs. Therefore, LMD has attracted widespread attention in manufacturing new parts and repairing damaged superalloy components [3, 4].

ATI 718Plus alloy, henceforth denoted as 718Plus, is a precipitation-strengthened Ni-based superalloy that exhibits superior properties such as strength, hardness, corrosion resistance, and creep resistance compared to Inconel 718 [5, 6]. Its maximum operational temperature extends to 704 °C, a feat primarily due to the refined alloy composition. On the basis of the composition of Inconel 718, 9 wt% Co and 1 wt% W are added to improve the high-temperature stability, while adjusting the Al + Ti content and Al/Ti ratio, so that the strengthening phase γ'' transformed to γ' phase. While maintaining the original machinability and weldability, the critical service temperature of the alloy has been elevated by 50 °C in comparison with Inconel 718. [7].

In order to explore the optimal properties of the alloys, researchers have been dedicated to diverse approaches, encompassing additive manufacturing process parameters

✉ Jide Liu
  jdliu@imr.ac.cn

✉ Jinguo Li
  jgli@imr.ac.cn

1 Key Laboratory for Anisotropy and Texture of Materials (MOE), School of Materials Science and Engineering, Northeastern University, Shenyang 110819, China

2 Research Center for Metallic Wires, Northeastern University, Shenyang 110819, China

3 Shi-Changxu Innovation Center for Advanced Materials, Institute of Metal Research, Chinese Academy of Sciences, Shenyang 110016, China

[8–10], heat treatment processes [11–14], and composition modulation [15–17]. Ma et al. [18] investigated direct laser fabrication (DLF) of Inconel 718 alloy, discovering that lower energy input contributed to lower Laves phase volume fraction and increased precipitation of γ' and γ'' phases. However, the lower energy input led to an increase in porosity, which in turn affected the density of the alloy. Hu et al. [19] studied the effect of solution treatment temperature on the microstructure and mechanical properties of laser solid forming (LSF) Inconel 625 alloy. Their results showed that increasing the solid solution treatment temperature resulted in a decrease in the volume fraction of the Laves phase and an increase in the elongation. Complete recrystallization of the alloy occurred when the solid solution treatment temperature reached 1200 °C [20]. Although high-temperature heat treatment can help to optimize the microstructure and mechanical properties of alloys, for some precision parts with high requirements, high-temperature heat treatment can easily lead to local deformation, which is completely unacceptable.

Compositional modulation stands out as a potent strategy for enhancing the mechanical properties of LAM Ni-based superalloys. Zhao et al. [21] added Zr to Haynes 230 alloy by additive manufacturing. The results show that Zr can help to eliminate cracks, while the continuous $Ni_{11}Zr_9$ network layer was able to act as a "skeleton" to significantly improve the yield strength of as-deposited samples. Sun et al. [22] fabricated Inconel 718 alloy with different W contents by laser cladding (LC) and investigated the effect of W content on the microstructure and mechanical properties of the alloy. They found that the Laves phase volume fraction and dislocation density in the alloy gradually increased with the increase in W content, but the elongation decreased significantly. Zhang et al. [23] investigated the effect of Al on the microstructure and microhardness of LAM Inconel 718 alloy. Their results showed that an increase in Al content promoted increased Nb elemental segregation, leading to an increase in the Laves phase volume fraction. When 5 wt% Al was added, the simulation results showed the precipitation of NiAl phase in the alloy, which was not observed in the experiments. In addition, the microhardness increased with increasing Al content. Although researchers have done a lot of research on the mechanism of action of Al element,

there are still some details that have not been clarified and deserve discussion in detail.

To meticulously design the microstructure and improve the mechanical properties of the alloy, a detailed investigation into the mechanisms of various alloying elements is imperative. In this work, the as-deposited 718Plus alloy with various Al additions was fabricated by LAM, the microstructure evolution was analyzed, and the influence mechanism of mechanical properties was discussed.

2 Experimental

In the present study, a forged 718Plus alloy plate, measuring 20 mm×20 mm×20 mm in length, width, and height, respectively, was employed as the substrate. Prior to the printing process, the substrate was polished utilizing 400 grit sandpaper and then ultrasonically cleaned using acetone to remove surface impurities. The compositions of the alloy powders at different Al contents (1 wt%, 3 wt% and 5 wt%) are shown in Table 1. The alloy powders were fabricated using plasma rotating electrode process (PREP), and their morphology and particle size distribution are shown in Fig. 1. The powders exhibit a relatively clean surface, with a highly spherical shape and no hollow or satellite particles. The particle size range of the powder is 45–106 μm. LMD of 718Plus alloy was performed on a coaxial powder delivery system with argon protection. The specific process parameters for LMD are listed in Table 2.

Figure 2a shows the macroscopic morphology of LAM 718Plus alloy with different Al content. Microstructure samples were obtained by cutting the alloy using a wire electrical discharge machining, as shown in Fig. 2b. The alloy was subjected to standard metallographic preparation procedures. The microstructure of the alloy was observed using an optical microscope (OM, Axio Observer 3 m) and a scanning electron microscope (SEM, Thermo Scientific Apreo 2C). X-ray diffraction was utilized to identify the precipitation phases within the alloy. The element concentration and distribution were analyzed by electron probe micro-analyzer (EPMA, JXA-8530F). Transmission electron microscopy (TEM) specimens examined in a JEOL ARM 200F microscope in the bright field at an accelerating voltage of 200 kV. Thermal Calc 2023a software using the TCNI10 database was used to calculate the precipitated phase composition and solidification behavior of the alloy. Microhardness of alloys

Table 1 Chemical compositions of 718Plus alloy powder (wt%)

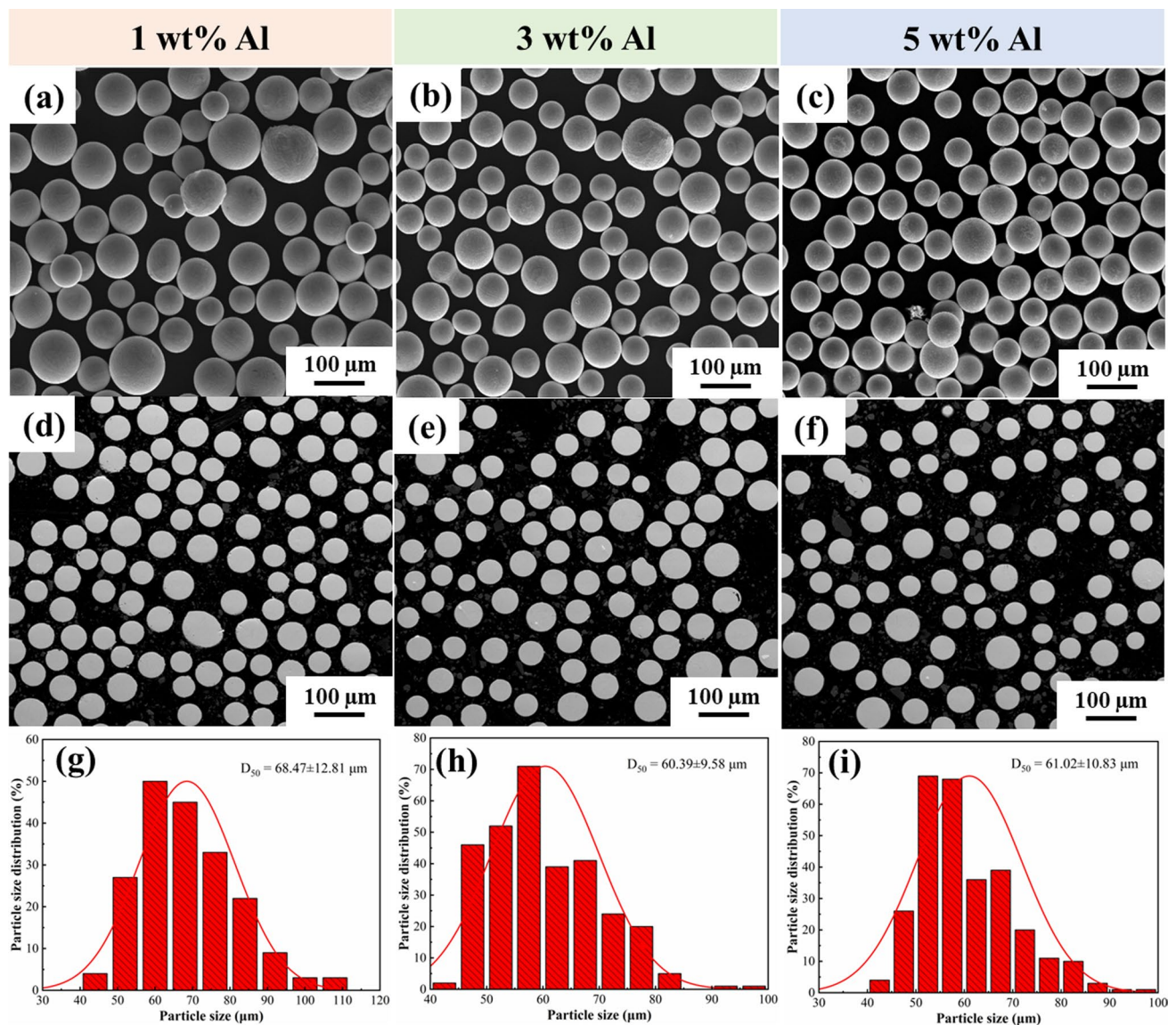| Alloy	Al	Ti	Nb	W + Mo + Cr + Co	Fe	C	Ni
1 wt% Al	1.65	0.8	5.6	30–33	9.9	0.024	Bal.
3 wt% Al	3.65	0.8	5.6	30–33	9.9	0.024	Bal.
5 wt% Al	5.65	0.8	5.6	30–33	9.9	0.024	Bal

Fig. 1 Surface morphology, cross-sectional morphology, and particle size distribution of 718Plus alloy powders with different Al additions: **a**, **d**, **g** 1 wt% Al; **b**, **e**, **h** 3 wt% Al; **c**, **f**, **i** 5 wt% Al

Table 2 Parameters for the LMD process

Laser power (W)	Scanning speed (mm/s)	Powder feeding rate (g/min)	Spot diameter (mm)	Z-axis lifting height (mm)	Overlap (%)
900	8	7	2	0.7	50

with different Al contents was measured using a Vickers hardness tester with 100 g load for 15 s. The tensile tests were conducted using a CMT-30 electronic universal testing machine at room temperature.

3 Results

3.1 Microstructure

Figure 3 shows the OM images of as-deposited 718Plus alloy with different Al additions, revealing no crack formation. However, despite adjustments in processing parameters, pore elimination remains a challenge. The porosity of the three alloys is measured using Image Pro Plus (IPP) software to be 0.65%, 0.38%, and 0.36%, respectively, indicating that the as-deposited sample is nearly fully dense. In addition, the microstructure of the samples exhibits dendritic morphology and layer band structure (the single deposited pass or layer) can be observed in these specimens, as shown in Fig. 3d–f.
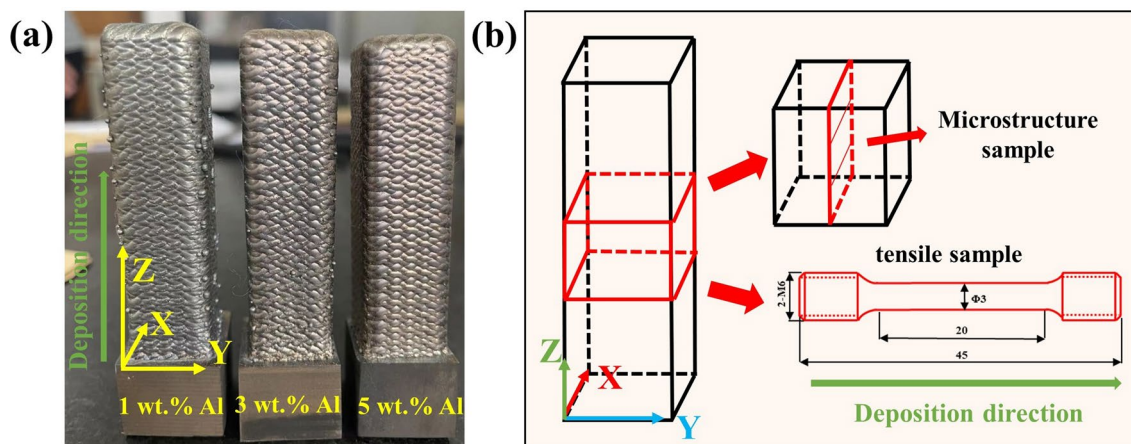
Fig. 2 As-deposited 718Plus alloy with different Al additions: **a** macroscopic morphology; **b** schematic diagram of microstructure and tensile sample
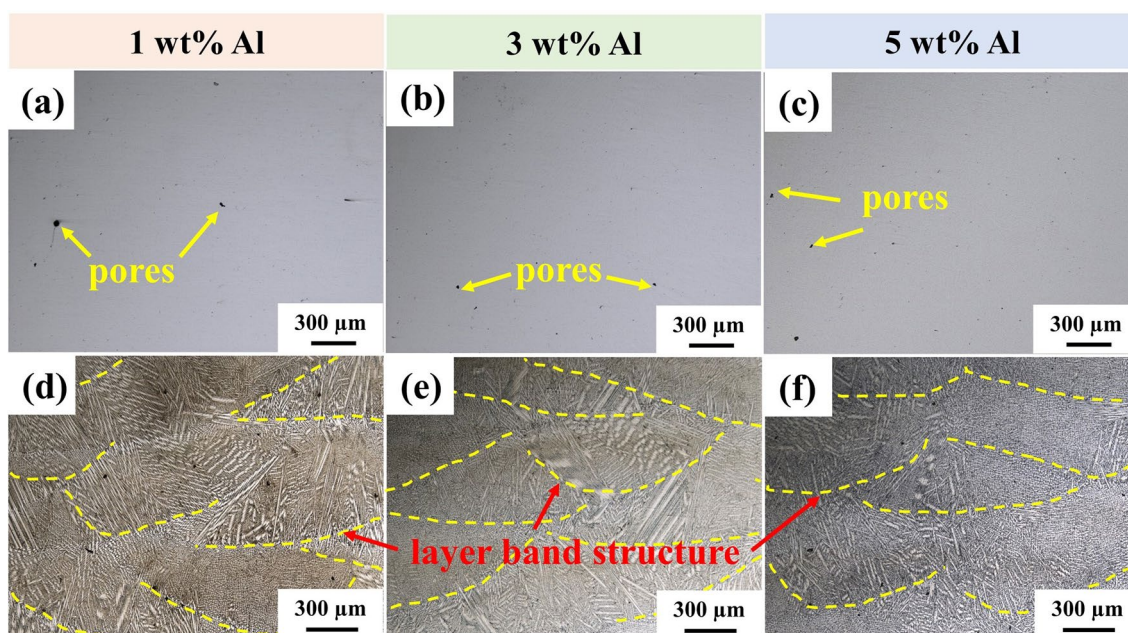

Fig. 3 OM images before and after corrosion of as-deposited 718Plus alloy with different Al additions: **a** and **d** 1 wt% Al; **b** and **e** 3 wt% Al; **c** and **f** 5 wt% Al

Figure 4 shows the XRD patterns of as-deposited 718Plus alloy with different Al additions. The alloy primarily consists of Laves phase, γ and γ' phases. The other phases in the alloy were not detected due to their low volume fraction. With increasing the Al content, the diffraction peak intensity of γ/γ' phase progressively increases, indicating that more γ' phase has been formed in γ matrix during the printing process. Concurrently, the decrease in diffraction peak angle means that the lattice constant of the γ' phase increases. It is worth noting that obvious peaks corresponding to the NiAl phase are detected in the pattern of 5 wt% Al-added 718Plus

alloy (Fig. 4b). Figure 5 shows the SEM images of as-deposited 718Plus alloy with different Al additions. A large number of white precipitates are formed at the interdendritic regions. To further determine the composition of the white precipitates, EPMA technology was utilized to analyze the element distribution, as shown in Fig. 6. The results indicate that the white precipitate phase is rich in Nb, Mo and poor in Ni and Al. Based on its composition and morphology, it can be determined that the phase is Laves phase [24]. In addition, enrichment of Ni and Al atoms is observed in the middle of the Laves phase in 5 wt% Al-added 718Plus
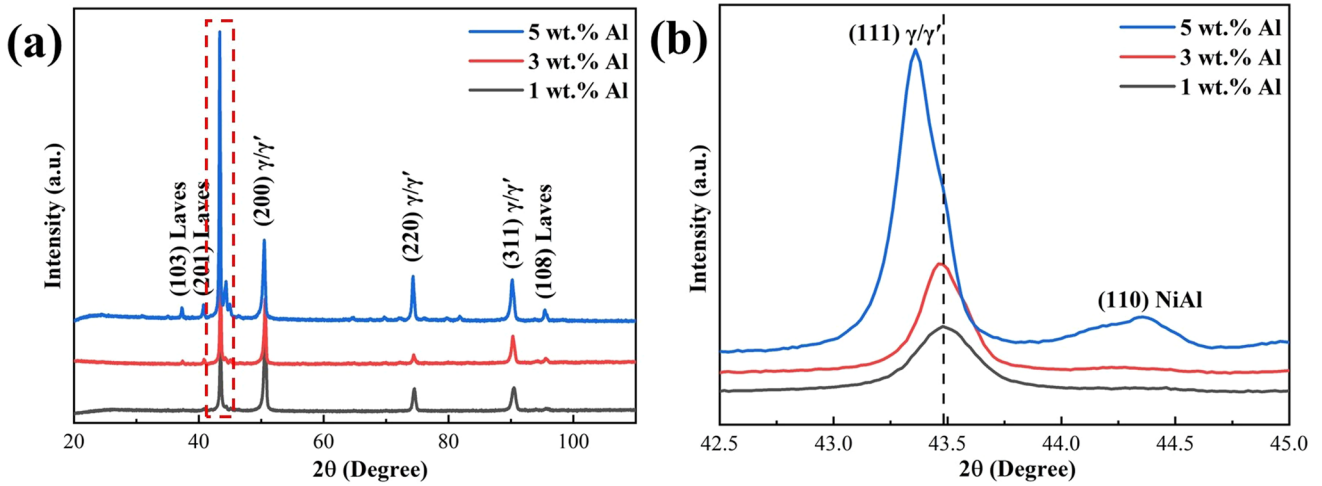
Fig. 4 **a** XRD patterns of as-deposited 718Plus alloy with different Al additions; **b** local magnification in **a**
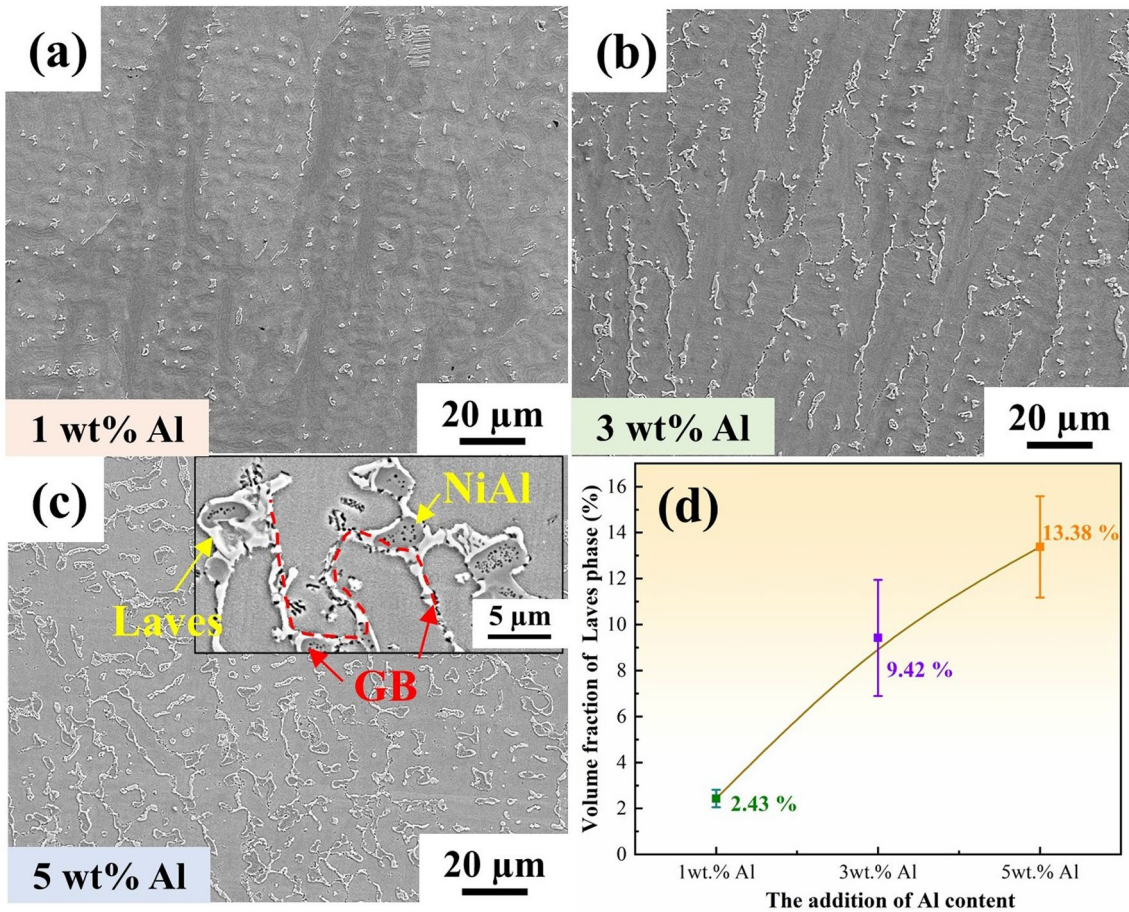

Fig. 5 Laves phase of as-deposited 718Plus alloy with different Al additions: **a** 1 wt% Al; **b** 3 wt% Al; **c** 5 wt% Al; **d** variation trend of Laves phase volume fraction in different samples

alloy, which was speculated to be NiAl phase in conjunction with the XRD results. With the increase in Al content, the Laves phase gradually transforms from block to chain-like distribution, and the Laves phase transforms to a continuous net-like distribution in the 5 wt% Al 718Plus alloy. Detailed statistics of laves phase volume fractions are performed
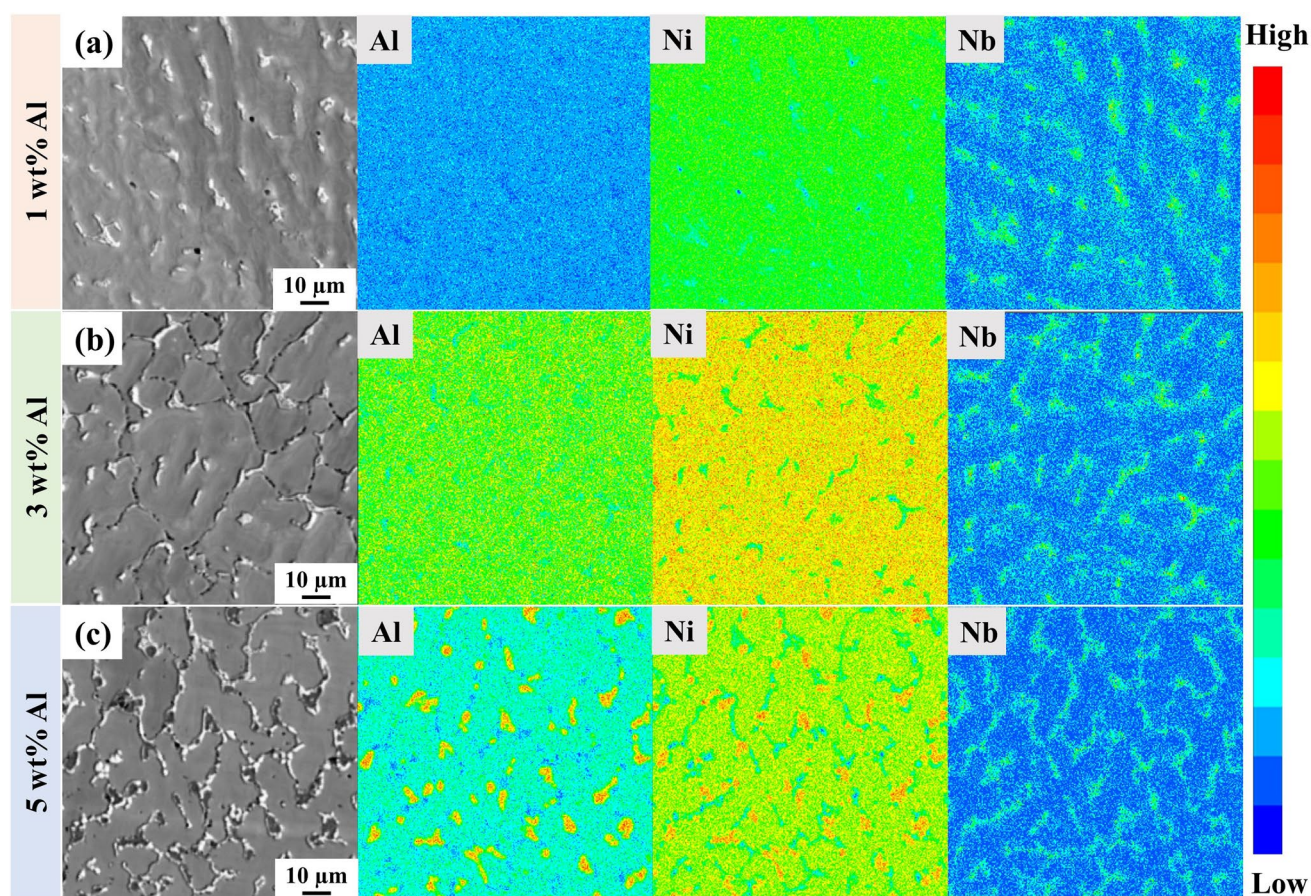
Fig. 6 EPMA mapping of as-deposited 718Plus alloy with different Al additions: **a** 1 wt% Al; **b** 3 wt% Al; **c** 5 wt% Al

using IPP software, as shown in Fig. 5d. With the increase in Al content, the volume fraction of Laves phase significantly increases. Zhang et al. [23] found through simulations and experiments that the segregation of Nb induced by Al increases the volume fraction of Laves phase, which is consistent with the results of this study.

By magnifying the microstructure of 718Plus alloy with different Al additions, as shown in Fig. 7, it is found that the η phase precipitates around the Laves phase and at grain boundary in 1 wt% Al-added 718Plus alloy, while no white η phase can be observed in both 3 wt% and 5 wt% Al-added 718Plus alloy. In addition, laser additive manufacturing is a layer-by-layer building process; the previously solidified regions undergo a continuous thermal cycle leading to the inherent heat treatment effect, which causes the atom to diffuse a sufficiently long enough distance. When the temperature is in the precipitation temperature range of γ' phase, it leads to γ' phase precipitation. Due to the tendency of Al element to segregate preferentially in the interdendritic region, the size of the γ' phase in the interdendritic region is slightly larger than that in the dendritic trunk, as shown in Fig. 7b and c. With the increase in Al content, the γ' phase

morphology gradually transforms from spherical to cubic, while the γ' phase size between the interdendritic and at the dendrite trunk tends to be the same, which will be discussed in detail later.

The microstructure of 1 wt% Al-added 718Plus alloy was investigated in detail by TEM. Figure 8a shows the high-resolution TEM image of the surface between Laves and η phases. Combined with the fast Fourier transform (FFT) images, the crystallographic orientation relationship between the Laves and η phases can be determined as: $(000\bar{1})_{\eta}\parallel(\bar{1}0\bar{1}0)_{Laves}$ and $[2\bar{1}\bar{1}0]_{\eta}\parallel[1\bar{2}1\bar{3}]_{Laves}$. In addition, the large bulk precipitated phases in the interdendritic region mainly include Nb, Ti, and C elements, and the corresponding selected area electron diffraction (SAED) pattern can identify the bulk phase as MC carbide (Fig. 8f). It is worth noting that spherical precipitates rich in Al and O are precipitated near the MC carbides, which cannot be identified by the corresponding SAED pattern due to their small average size. The spherical phase is presumed Al_2O_3 due to its lower Gibbs energy [25]. This may be due to oxygen contamination during powder preparation; a small amount of Al atoms combine with oxygen during the manufacturing process to
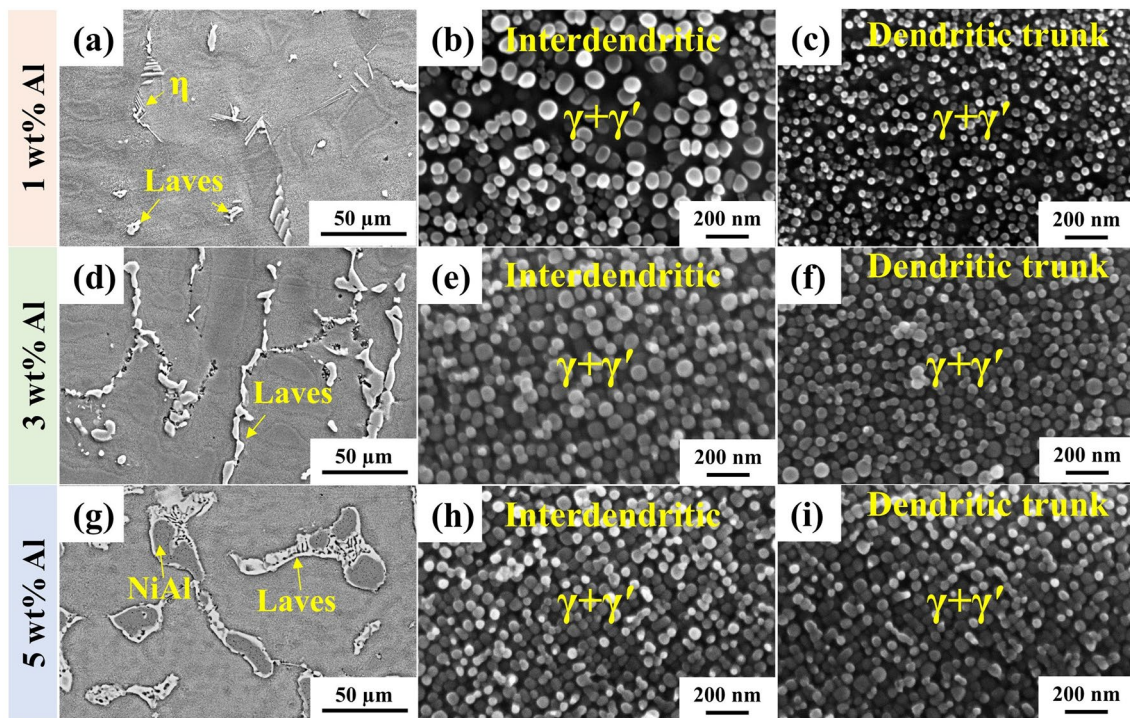
Fig. 7 Microstructures of as-deposited 718Plus alloy with different Al additions: **a–c** 1 wt% Al; **d–f** 3 wt% Al; **g–i** 5 wt% Al

form oxide particles, which can serve as heterogeneous nucleation sites for carbides [26]. It is reported [27] that the nanoscale oxides in the additive manufacturing alloy can hinder the movement of dislocations and grain boundaries, thereby affecting the mechanical properties of the built part.

3.2 Mechanical Properties

Room-temperature tensile test and Vickers microhardness test were used to investigate the effects of Al on the mechanical properties of 718Plus alloy. It can be seen from Fig. 9a that the microhardness gradually increases with the increase in Al content, and the microhardness of 5 wt% Al-added 718Plus alloy can reach up to 514 ± 8 HV. Figure 9b shows the engineering stress–strain curves of the as-deposited 718Plus alloy at different Al additions. It is interesting to note that the ultimate tensile strength shows an increasing and then decreasing trend with increasing Al content, reaching a maximum of 1075 ± 20 MPa for the 3 wt% Al-added 718Plus alloy. However, the elongation of the alloy exhibits a tendency to decrease precipitously. Due to the limited research on additive manufacturing of 718Plus alloy, the results of this work compared the as-deposited Inconel 718 alloy with different additive manufacturing techniques (Fig. 9c) [15, 22, 28–34]. Overall, three alloys have high strength and insufficient plasticity, with the 1 wt% Al-added 718Plus alloy having a better strength–plasticity match.

Figure 10 shows the fracture morphology of 718Plus alloy with different Al additions. The dendritic morphology is still retained for all fractured samples. The fracture surface of 1 wt% Al-added 718Plus alloy shows an obvious necking phenomenon, the fracture surface is uneven, and a large number of dimples are observed, showing obvious intergranular fracture characteristics. In contrast, the other two alloys have a relatively flat fracture surface with numerous cracks and no dimples observed, thus showing poor plasticity and obvious brittle fracture characteristics.

4 Discussion

4.1 Crack Susceptibility and Solidification Behavior

At present, the primary problem of alloy composition design in additive manufacturing is to avoid crack formation. Cracks in additively manufactured superalloys can be broadly categorized into two types: hot-tearing cracks and solid-state cracks. The freezing range (FR) is used as an important indicator of the propensity for hot-tearing crack tendency as follows [35]:

$$\mathrm{FR} = T_{\mathrm{Liquidus}}^{\mathrm{SG}} - T_{\mathrm{Solidus}}^{\mathrm{SG}}. \tag{1}$$
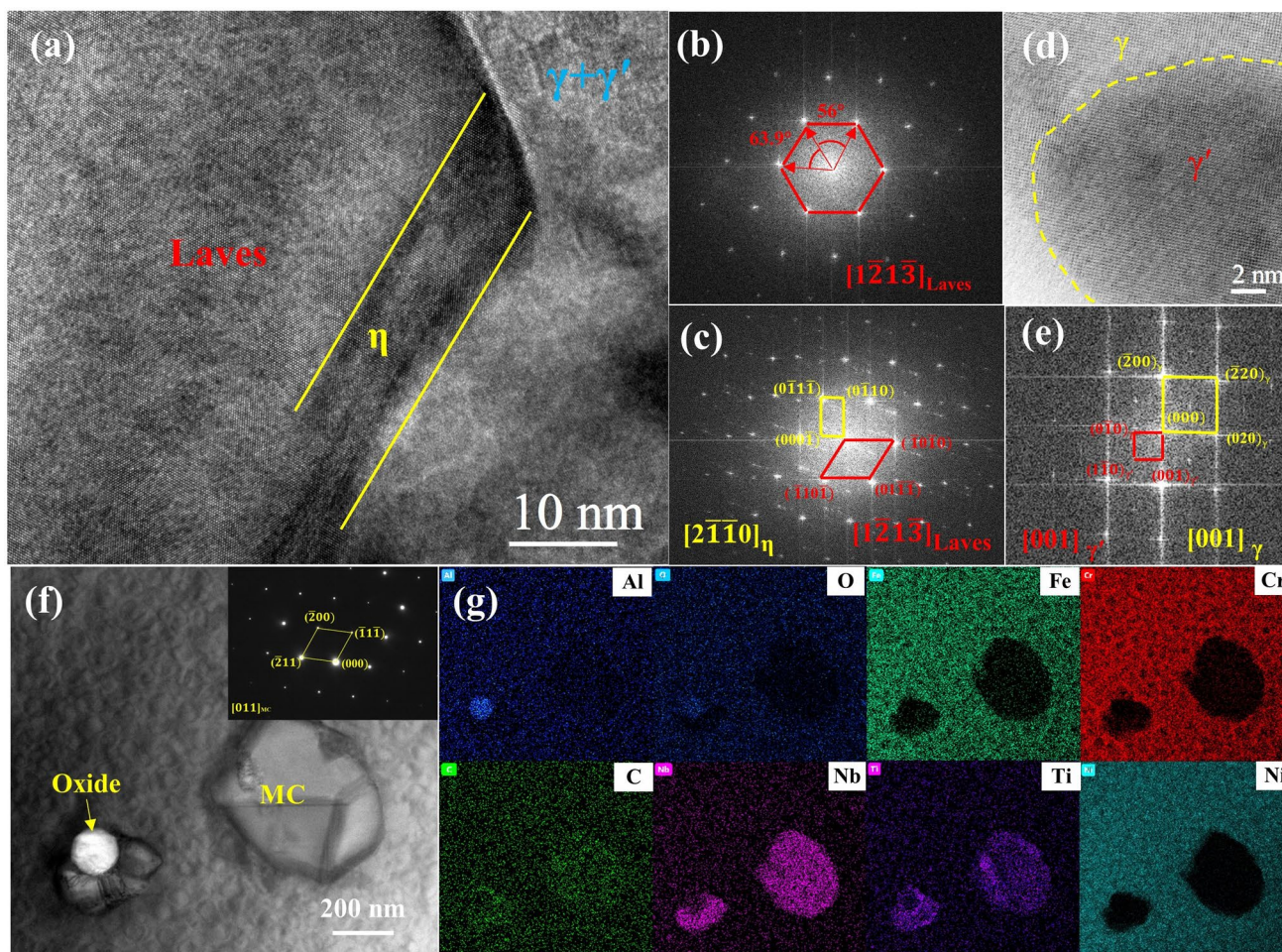
Fig. 8 Microstructures of 1 wt% Al-added 718Plus alloy: **a** high-resolution TEM image of the surface between the Laves and η phase; **b** FFT image of the Laves phase; **c** FFT image of the phase interface between the Laves and η phase; **d** high-resolution TEM image of the surface between the γ and γ′ phase; **e** FFT image of the γ′ phase; **f** TEM bright image of the oxide and *M*C carbide; **g** TEM-EDS elemental maps of **f**
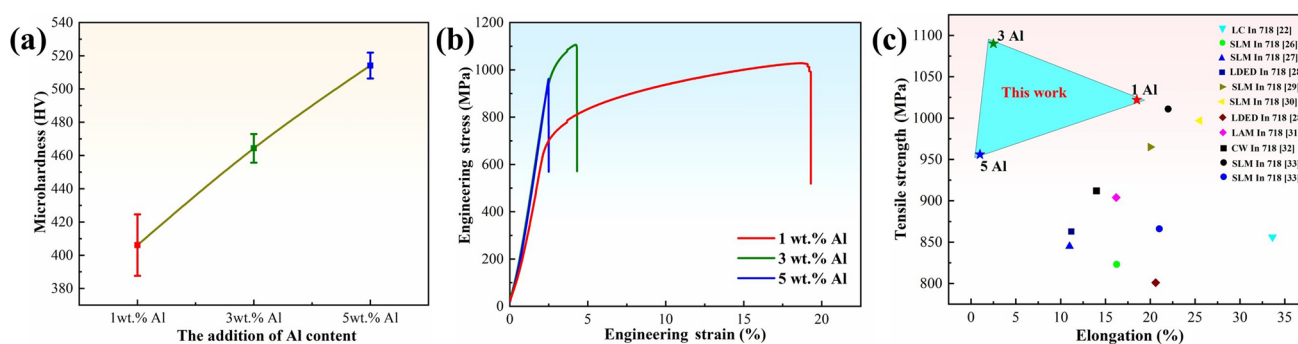

Fig. 9 Tensile properties of as-deposited 718Plus alloy with different Al additions: **a** Vickers microhardness; **b** engineering stress–strain curves; **c** compared with various types of as-deposited Inconel 718 alloy

where $T_{\text{Liquidus}}^{\text{SG}}$ and $T_{\text{Solidus}}^{\text{SG}}$ represent the liquidus and solidus temperature of Scheil–Gulliver solidifications, respectively, and $T_{\text{Solidus}}^{\text{SG}}$ is obtained by setting the terminal solid fraction

to 99%. The Scheil model of non-equilibrium solidification can effectively describe the solidification process of the alloy. The solidification pathways of 718Plus alloy with different Al contents were simulated utilizing Thermo Calc
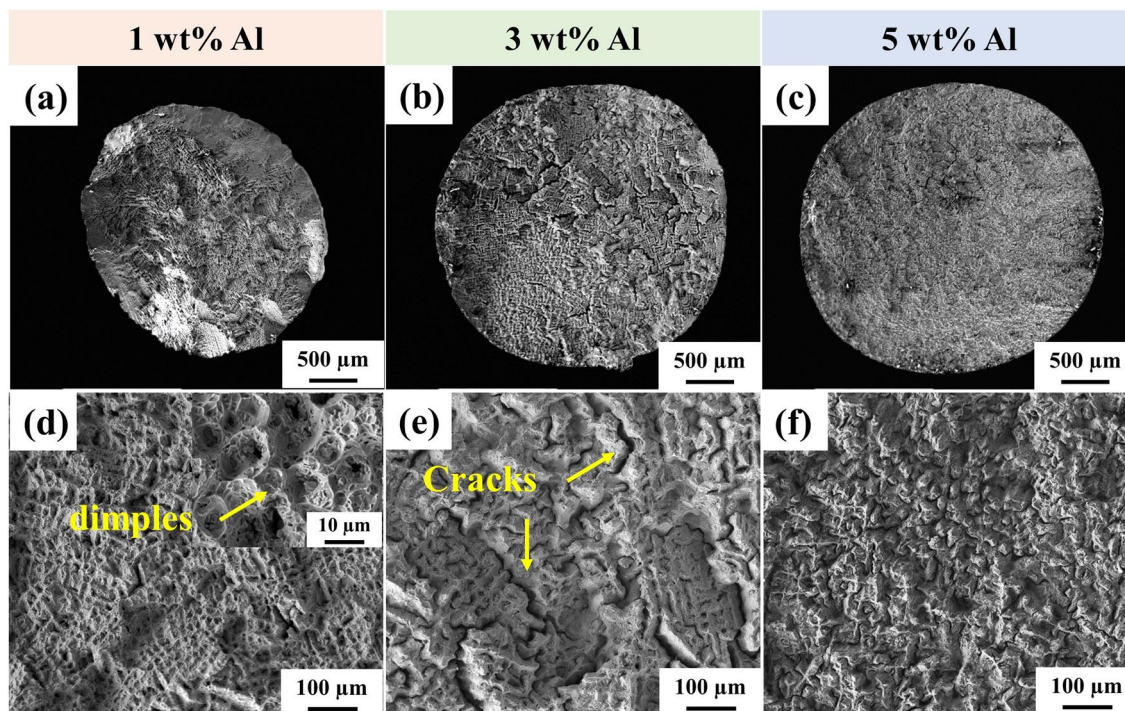
Fig. 10 Fracture morphologies of as-deposited 718Plus alloy with different Al additions: **a** and **d** 1 wt% Al; **b** and **e** 3 wt% Al; **c** and **f** 5 wt% Al

software, as shown in Fig. 11. It can be seen from the solidification curve that the FR decreases with the increase in Al content, which implies the decrease in mushy zone (liquid–solid mixture). The smaller FR helps the alloy pass through the high crack susceptibility microstructure quickly, which ultimately leads to the decrease in hot-tearing crack susceptibility.

The solid-state cracking (SAC) is associated with the precipitation of the γ' phase during thermal cycling or heat treatment. Reed et al. [36] evaluated the solid-state cracking tendency type of the alloys by comparing the contents of four precipitation strengthening elements (γ' phase forming elements), Al, Ti, Nb, and Ta (wt%). The index is as follows:

$$M_{sac} = W_{Al} + 0.5W_{Ti} + 0.3W_{Nb} + 0.15W_{Ta}. \tag{2}$$

where W_X is the weight fraction of alloy element X. According to Eq. (2), it can be calculated that the 5 wt% Al-added 718Plus alloy has the highest M_{sac} value. At the same time, the increase in Al content in the alloy can promote the formation of γ' phase and eutectic phase, leading to a greater propensity for solid-state cracking. This may be due to that the γ' phase does not precipitate completely in the as-deposited sample, which results in the non-formation of the solid-state crack. In this work, the effect of Al addition on crack sensitivity is contradictory, but no cracks were found in all samples, indicating that the control range of Al element is reasonable.
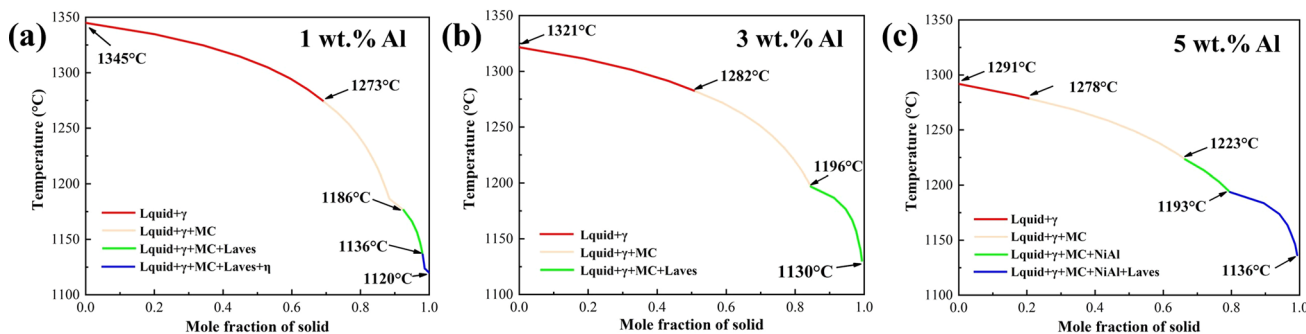

Fig. 11 Scheil solidification curves of as-deposited 718Plus alloy with different Al additions: **a** 1 wt% Al; **b** 3 wt% Al; **c** 5 wt% Al

To further verify the accuracy of the simulation results, the cooling curves of differential scanning calorimetry (DSC) were analyzed, as shown in Fig. 12. When 1 wt% Al is added, the initial solidification temperature is 1318 °C and the complete solidification temperature is 1169 °C. When 5 wt% Al is added, the initial melting temperature is 1265 °C and the complete melting temperature is 1172 °C. It indicates that the solidification range gradually narrows with the increase in Al content, which is consistent with the simulation results. It is worth mentioning that there is no endothermic peak corresponding to η phase at 1 wt% Al-added 718Plus alloy, which may be due to the low volume fraction of η phase. The second endothermic peak in the heating curve of 5 wt% Al-added 718Plus alloy is 1217 °C, which corresponds to the dissolution temperature of NiAl phase; this indicates that the formation of NiAl phase is an intermediate process of solidification. In the last solidification stage, elements such as Nb and Mo will segregate at the interdendritic region. Meanwhile, the formation of NiAl phase further promotes the segregation of Laves phase forming elements. Dupont et al. [37, 38] believe that during the solidification process of Nb-bearing superalloys, when the Nb content in the liquid phase exceeds 23.1 wt%, Laves phase will be formed. Therefore, the Laves phase is formed as the eutectic phase at the last solidification stage. The solidification paths of precipitates in 5 wt% Al-added 718Plus alloy can be summarized by DSC curves and simulation results: liquid → liquid + γ → liquid + γ + MC → liquid + γ + MC + NiAl → liquid + γ + MC + NiAl + Laves.

4.2 Precipitation Mechanism of NiAl Phase

Figure 13a–c shows the simulated phase diagrams for 718Plus alloy with different Al additions. The volume fraction of γ′ phase in the alloy does not show a linear
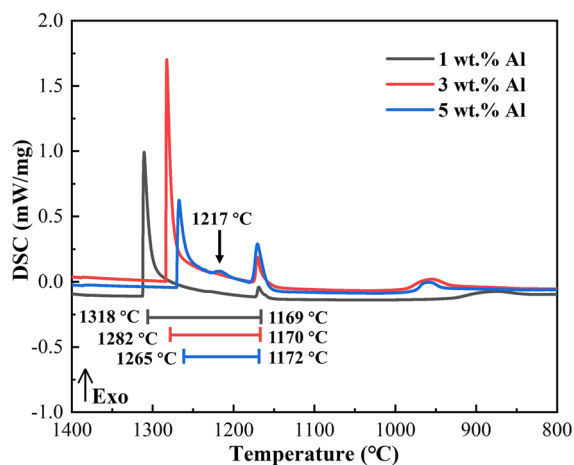

Fig. 12 Cooling curves of DSC of as-deposited 718Plus alloy with different Al additions

increase with increasing Al content, while precipitation of NiAl phase is found in 5 wt% Al-added 718Plus alloy. This suggests that the contents of Al atoms directly influence the formation of the NiAl phase. According to the classical nucleation theory, the nucleation barrier ΔG^* can be expressed as follows [39]:

$$\Delta G^* = \frac{16}{3} \pi \frac{\gamma^3}{\Delta G_V^2}. \tag{3}$$

where G_V is the onset driving force for precipitation and γ is the interfacial energy between the precipitate and the γ matrix. With the increase in Al content, the interfacial energy between the NiAl phase and the γ matrix does not change significantly and is at a low level, but the normalized driving force gradually increases, as shown in Fig. 13d and e. According to Eq. (3), the nucleation barrier of the NiAl phase decreases, and thus, the observation of NiAl phase in the 5 wt% Al-added 718Plus alloy is not surprising.

To further elucidate the formation of NiAl phase, the phase diagram of the Ni–Al binary alloy was simulated (Fig. 13f). When the amount of Al added is low, the Ni₃Al phase is first formed in γ matrix. With the increase in Al content, the solidification path changes accordingly. During solidification, Al atoms tend to segregate in the interdendritic region, when the Al content in the liquid phase reaches around 14 wt%. It results in the solid solution effects in the γ matrix reaching its upper solubility limit, known as the supersaturation. This supersaturation provides nucleation sites for the precipitation of the NiAl phase, which leads to the formation of the NiAl phase first, followed by the Ni₃Al phase. The conditions for the formation of NiAl phase are satisfied from the thermodynamic analysis. In addition, grain boundaries belong to surface defects, which provide energetic undulations for the formation of new phases and can provide nucleation sites for new phases. At the same time, grain boundaries can provide a fast channel for element diffusion, which is beneficial to the growth of new phases. It has been demonstrated that when only considering interface energy, the nucleation energy required to form an incoherent new phase nucleus at the grain boundary is less than one-third of that of inside the grain [40]. It is indicated that grain boundaries are directly involved in the precipitation reaction of NiAl phase. Furthermore, the crystallographic orientation relationships of the NiAl and γ matrix in 5 wt% Al-added 718Plus alloy were investigated in our previous work [41]. The NiAl phase and the γ matrix belong to incoherent interface with high nucleation barriers, and thus, the grain boundaries are the only suitable sites for the heterogeneous nucleation of the NiAl phase, as shown in Fig. 5c.
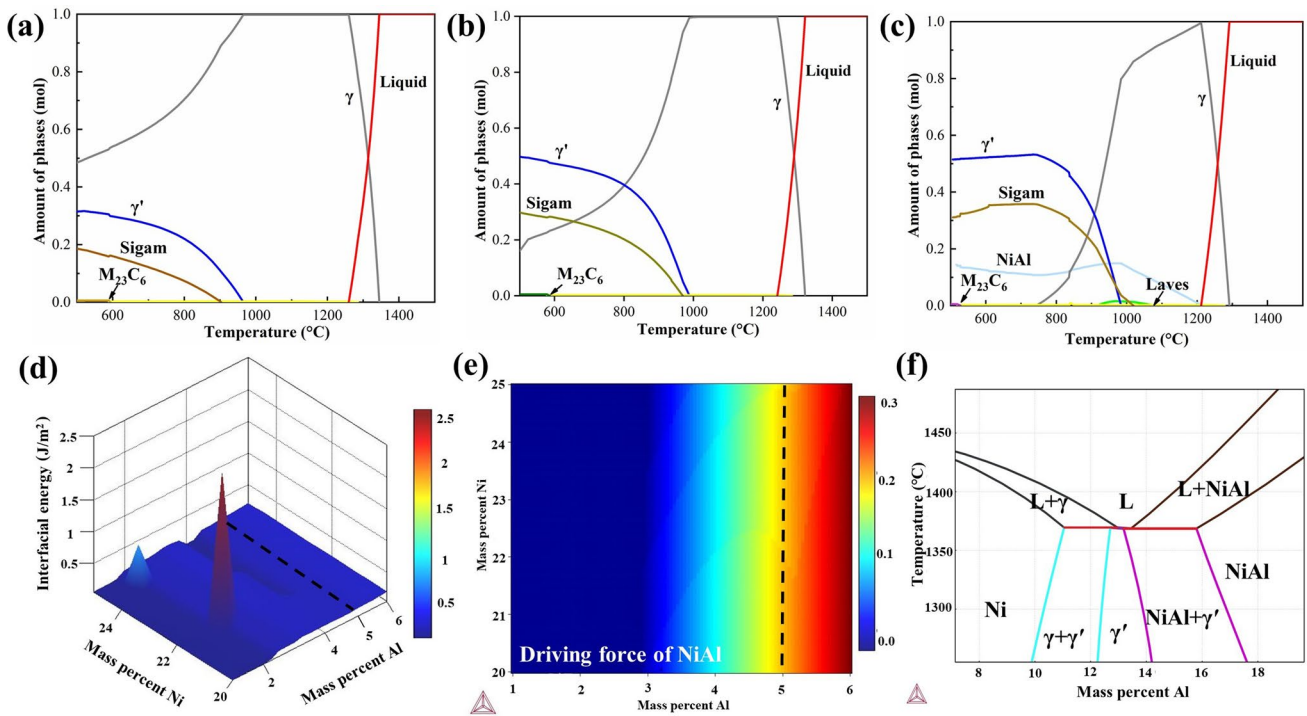
Fig. 13 CALPHAD analyses based on TCNI10 database: **a** phase diagrams of 1 wt% Al-added 718Plus alloy; **b** phase diagrams of 3 wt% Al-added 718Plus alloy, **c** phase diagrams of 5 wt% Al-added 718Plus alloy; **d** the interfacial energy between NiAl phase and the γ matrix; **e** normalized driving force between NiAl phase and the γ matrix; **f** the phase diagram of Ni–Al binary alloy

4.3 Microstructure Evolution and Segregation Behavior

Additive manufacturing has a faster solidification rate than traditional casting technology, and the actual solidification process is still difficult to reach the equilibrium solidification state, and the phenomenon of elemental segregation still exists. The alloy composition ratio between interdendritic and dendritic trunk was used as the elemental segregation coefficient $K_i = C^i_{dendrite}/C^i_{interdendrite}$, and the statistical results are shown in Fig. 14. With the increase in Al content, the elemental segregation coefficient gradually tends to unity, indicating the weakening of elemental segregation, which may be related to the precipitation of NiAl phase and the increase in the volume fraction of Laves phase. The nucleation and growth of NiAl and Laves phases consume a large amount of Nb, Mo, Ni, and Al atoms in the interdendritic region, leading to a decrease in the content of those elements enriched in the interdendritic region. Therefore, the contents of elements in interdendritic and dendritic trunks tend to be the same after the solidification of the alloy (Fig. 14). In addition, the size and morphology of the γ′ phase in the interdendritic and dendritic trunk regions of the 5 wt% Al-added 718Plus
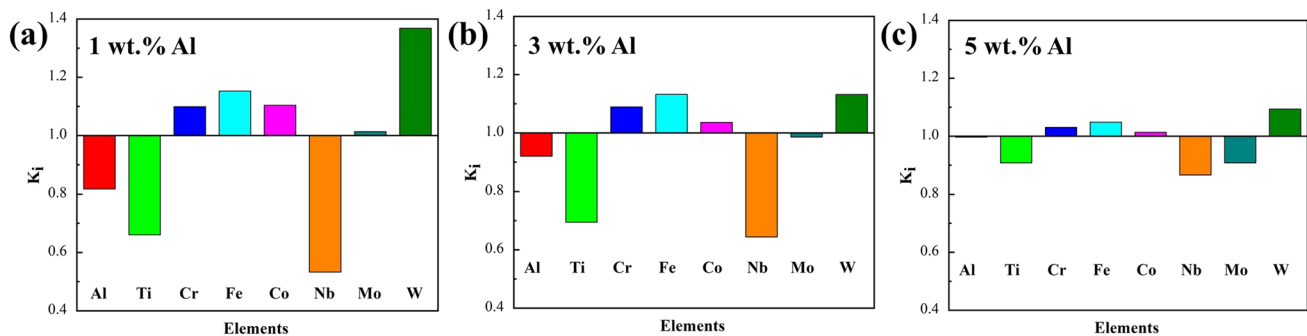

Fig. 14 Elemental segregation of as-deposited 718Plus alloy with different Al additions: **a** 1 wt% Al; **b** 3 wt% Al; **c** 5 wt% Al

alloy tend to be consistent (Fig. 7), further confirming the rationality of the above analysis.

It is well known that the morphology of the γ' phase is mainly closely related to the interfacial energy and elastic strain energy [42–44]. Many literatures have reported that the γ/γ' lattice misfits also affect the morphology of γ' phase [45]. Zhang et al. [46] found that increasing the aging temperature led to a decrease in the γ/γ' lattice misfits, but the spherical morphology of the γ' phase of the HT700T Ni–Fe based superalloy did not change. Guo et al. [47] found that the γ/γ' lattice misfits increased with the aging time, and the γ' phase morphology changed from near-spherical to near cubic in 718Plus alloy. In this experiment, the γ/γ' lattice misfits of alloys with different Al contents were measured by XRD. Due to the close lattice constants of the γ matrix and γ' phases, it is necessary to properly separate the (111) diffraction peaks obtained from the XRD, and the results are shown in Fig. 15a-c. The lattice parameters of the γ matrix and γ' phase were calculated using the Bragg equation and assuming cubic symmetry from the location of the peaks in the diffraction angle 2θ according to the following equation:

$$a = \frac{\lambda\sqrt{h^2+k^2+l^2}}{2\sin\theta}. \tag{4}$$

where λ is wavelength of X-rays (in the study, $\lambda = 0.154056$ nm) and $(h\,k\,l)$ is the Miller indices of the lattice plane under investigation. The following equation is used to calculate the γ/γ' lattice misfits δ[48]:

$$\delta = \frac{2\left(a_{\gamma'} - a_{\gamma}\right)}{\left(a_{\gamma'} + a_{\gamma}\right)}. \tag{5}$$

where $a_{\gamma'}$ and a_{γ} correspond to the lattice parameters of the γ' phases and γ matrix, respectively. The results of lattice parameters of the γ and γ' and γ/γ' lattice misfits of the alloy at different Al contents are shown in Fig. 15d and Table 3. The results show that the γ/γ' lattice misfits gradually increase from 0.05247 to 0.21548% with the addition of Al content, which is due to the preferential partitioning of Al into the γ' phase resulting in the increase in the lattice parameter of the γ' phase. The morphology of γ' phase in alloys with large lattice misfits is mainly controlled by
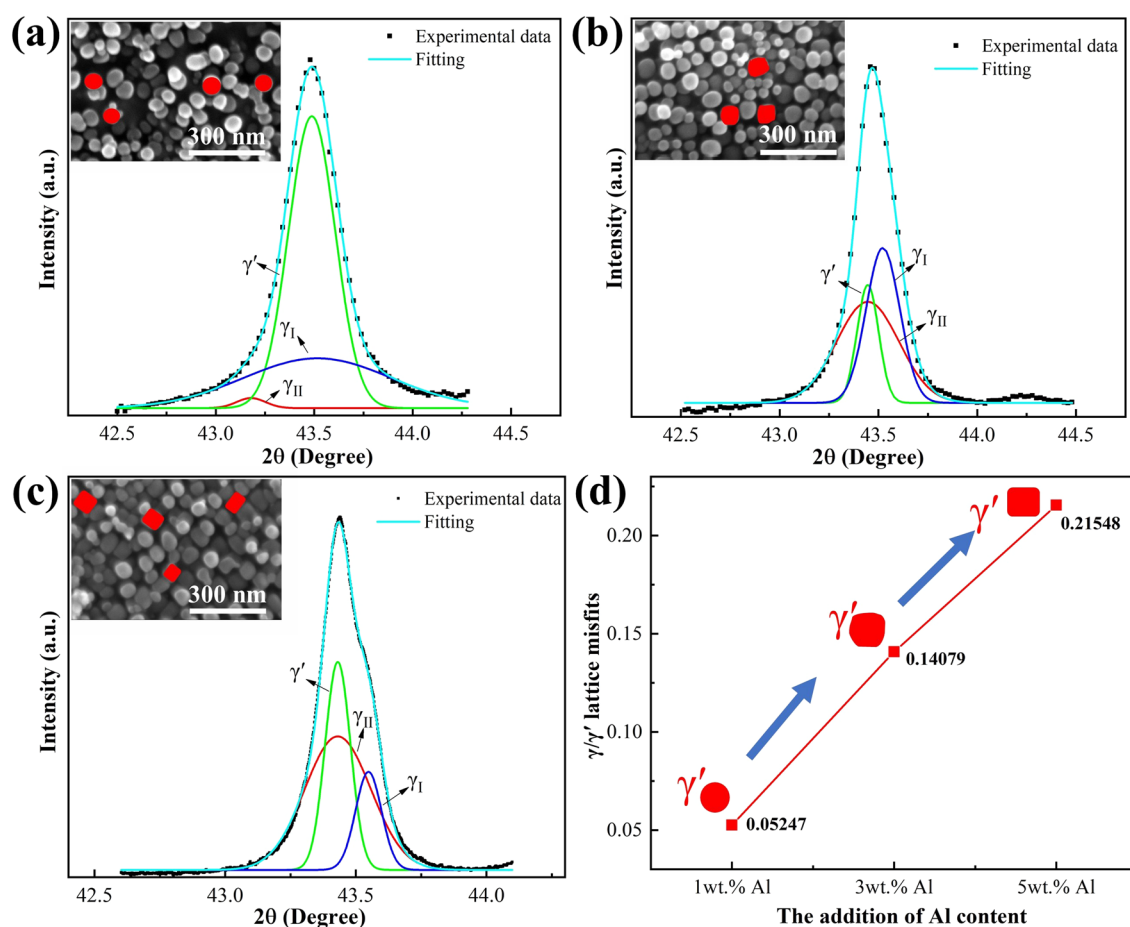

Fig. 15 Profiles of diffraction peaks (111) fitting results and γ/γ' lattice misfits of as-deposited 718Plus alloy with different Al additions: **a** 1 wt% Al; **b** 3 wt% Al; **c** 5 wt% Al; **d** γ/γ' lattice misfits

Table 3 Lattice parameters of the γ and γ' and the γ/γ' lattice misfits of as-deposited 718Plus alloy with different Al additions

Sample	1 wt% Al	3 wt% Al	5 wt% Al
$a_{\gamma'}$ (nm)	0.19379	0.19394	0.19399
a_{γ} (nm)	0.19368	0.19366	0.19357
δ (%)	0.05247	0.14079	0.21548

elastic strain energy. Due to the anisotropy of the crystals, the <001> orientation has the lowest elastic modulus, and thus, the γ' phase gradually shows a cubic distribution. Previous studies [49] have shown that a higher γ/γ' lattice misfits

will favorably promote the formation of a cubic γ' phase, which is consistent with the results of this paper.

A corresponding schematic diagram was drawn to illustrate the microstructure evolution process and element segregation behavior of the alloy, as shown in Fig. 16. According to thermodynamic calculations and DSC curves, it can be seen that the narrowing of the solidification temperature range with the increase in the Al element implies a shortening of the solidification time. According to Kurz and Fisher's (KF) model [50], the primary dendrite arm spacing (λ) can be expressed in the equation:
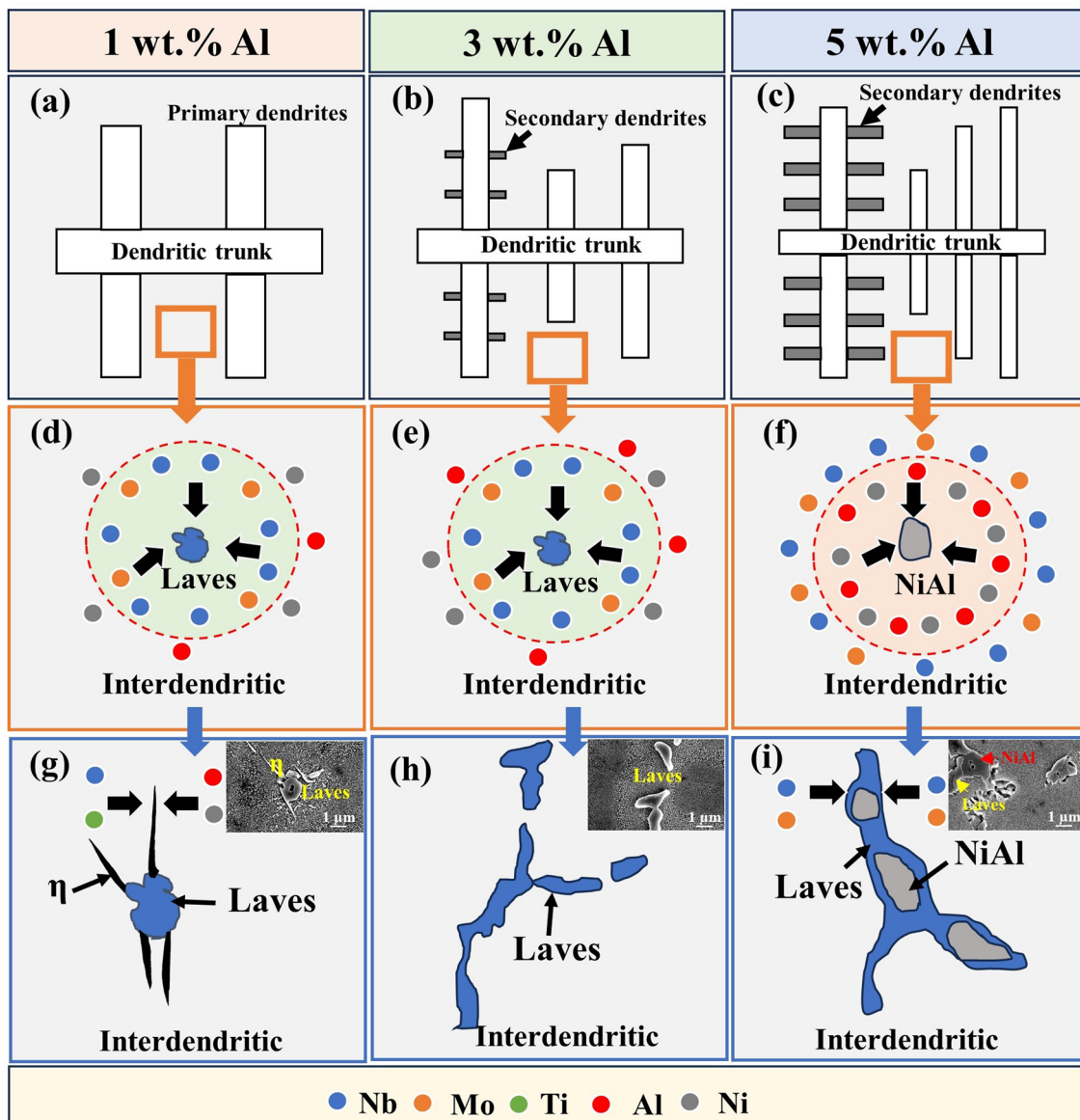

Fig. 16 Schematic diagram of microstructure evolution of as-deposited 718Plus alloy with different Al additions: **a**, **d**, **g** 1 wt% Al; **b**, **e**, **h** 3 wt% Al; **c**, **f**, **i** 5 wt% Al

$$\lambda = \sqrt{\frac{3\Delta T_0 R}{G}}. \tag{6}$$

where R is the dendrite tip radius, G is the temperature gradient and ΔT_0 is the non-equilibrium solidification range. According to Eq. (6), the primary dendrite spacing decreases with the solidification temperature range decreases as shown in Fig. 16a–c.

In the later stages of solidification, the 1 wt% and 3 wt% Al-added 718Plus alloy is enriched with elements such as Nb, Ti, and Mo in the interdendritic region, which directly led to the eutectic reaction of $L \rightarrow \gamma + \mathrm{Laves}$ [24, 51]. In contrast, the 5 wt% Al-added 718Plus alloy first precipitates the NiAl phase in the γ-matrix, and the formation mechanism of the NiAl phase is analyzed in detail in Sect. 4.2. The laves phase volume fraction in 1 wt% Al-added 718Plus alloy is low, and the remaining Nb and Ti elemental contents in the liquid phase are high enough to satisfy the thermodynamic nucleation conditions for the η phase. However, the volume fraction of the Laves phase increases significantly with increasing Al content, which results in a low content of η phase forming elements Nb in the residual liquid phase, which does not provide η phase nucleation sites. Therefore, 3 wt% and 5 wt% Al-added 718Plus alloy was not observed η phase precipitation (Fig. 16 h and i).

4.4 Influence of Al on Mechanical Properties

It is well known that the Laves phase has a topologically close-packed (TCP) structure with high coordination number and vacancy utilization, and dislocation nucleation and slip are very difficult, resulting in the Laves phase usually having a high hardness [11, 52]. With the increase in Al content, the increase in the volume fraction of Laves phase and γ' phase is the main reason for the increase in microhardness, as shown in Fig. 17. Stevens et al. [53] found in their study of direct laser deposition of 718 alloys that an increase in the volume fraction of Laves phase directly led to an increase in the microhardness of the alloy. In this work, the main considerations are solid solution strengthening, precipitation strengthening, and grain boundary strengthening, which play a decisive role in alloy strength.

It is worth mentioning that the Laves phase consists of a large number of solid solution elements such as Nb and Mo, so the formation of a large number of Laves phases will weaken the solid solution strength of the alloy. At the same time, the large area distribution of Laves phase seriously affects the interfacial stability with the γ matrix, and thus, the Laves phase is the main pathway for crack initiation and extension, as shown in Fig. 17. The γ' phase mainly contributes to the precipitation strengthening of the alloy, and the γ' phase volume fraction exhibits a trend of rapid increase followed by a slow increase, indicating that the precipitation strengthening contribution values of the 3 wt% and 5 wt% Al-added 718Plus alloy are essentially equivalent. In addition, with reference to previous research in additive manufacturing of Inconel 718 alloy [23], the increase in Al content did not change the orientation and quantity of grain boundaries, so the contribution value of grain boundary strengthening of the alloy remained unchanged. By summarizing, the strength contribution values of different alloys ultimately leads to a trend of increasing and then decreasing
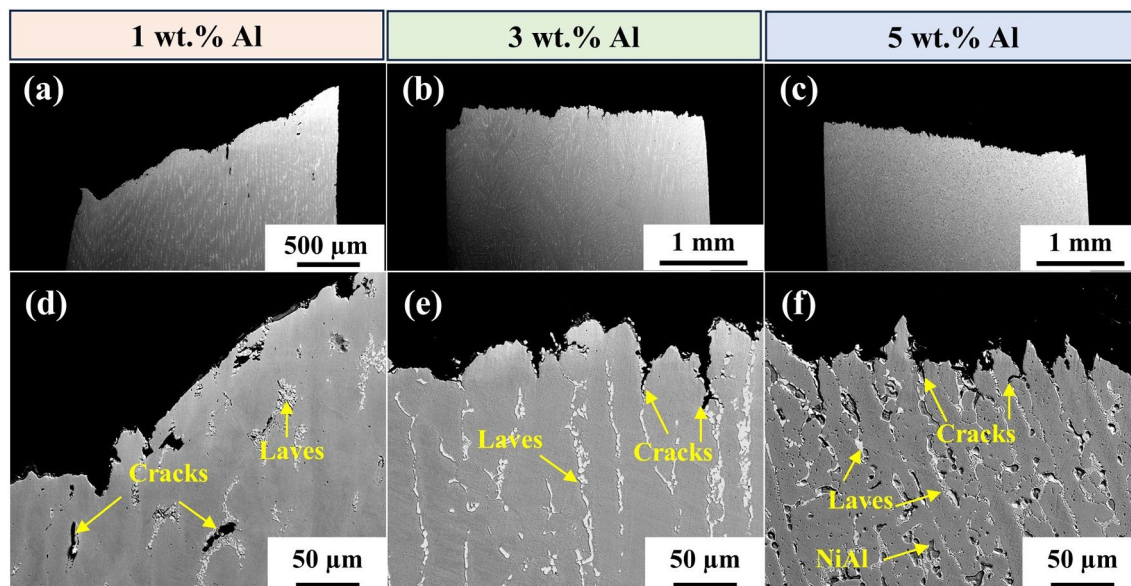

Fig. 17 Longitudinal sections of fracture surfaces after tensile testing of 718Plus alloy in the as-deposited state with different Al additions: **a** and **d** 1 wt% Al; **b** and **e** 3 wt% Al; **c** and **f** 5 wt% Al

tensile strength, as shown in Fig. 9. In addition, the severe decrease in plasticity of the alloy can be attributed entirely to the increase in the volume fraction of Laves phase. In particular, the NiAl phase precipitated within 5 wt% Al-added 718Plus alloy, which is a hard and brittle phase in superalloys, which accelerates the initiation and propagation of the crack, leading to the direct failure of the alloy before reaching the yield strength [54].

5 Conclusions

In this study, the effect of Al on the microstructural evolution and mechanical properties of additively manufactured 718Plus alloy was investigated. The main conclusions are as follows:

1. Simulation and experimental results show that the increase in Al content leads to the narrowing of the FR of the alloy. At the same time, the Al addition has diametrically opposite effects on the susceptibility to hot-tearing and solid-state cracking. In addition, the solidification path of the 5 wt% Al-added 718Plus alloy was summarized: liquid $\rightarrow$ liquid $+\gamma \rightarrow$ liquid $+\gamma+M$C $\rightarrow$ liquid $+\gamma+M$C $+$ NiAl $\rightarrow$ liquid $+\gamma+M$C $+$ NiAl $+$ Laves.

2. The increase in volume fraction of the γ' and Laves phases is promoted with increasing Al content, while the formation of the η phase is suppressed. The addition of Al increases the γ/γ' lattice misfits, leading to the transformation of the γ' phase from spherical to cubic. The NiAl phase precipitates in 5 wt% Al-added alloy, and the grain boundary provides the nucleation site for NiAl phase. In addition, the precipitation of the NiAl phase and the increase in the volume fraction of the Laves phase lead to a weakening of the interdendritic and dendritic trunk elemental segregation of the alloy after the completion of solidification.

3. With the Al content increases, the increase in the volume fraction of Laves phase and γ' phase leads to an increase in microhardness from 406 to 514 HV, and the tensile strength first increases and then decreases. The hard and brittle Laves phase and NiAl phase are responsible for the sharp deterioration of the alloy plasticity.

Declarations

Conflict of interest The authors declare that they have no known competing financial interests or personal relationships that could have appeared to influence the work reported in this paper.

References

[1] W.E. Frazier, J. Mater. Eng. Perform. **23**, 1917 (2014)
[2] Md. Shahwaz, P. Nath, I. Sen, J. Alloys Compd. **907**, 164530 (2022)
[3] R. Wang, W. Wang, G. Zhu, W. Pan, W. Zhou, D. Wang, F. Li, H. Huang, Y. Jia, D. Du, A. Dong, D. Shu, B. Sun, J. Alloys Compd. **762**, 237 (2018)
[4] P. Guo, B. Zou, C. Huang, H. Gao, J. Mater. Process. Technol. **240**, 12 (2017)
[5] G.A. Zickler, R. Radis, R. Schnitzer, E. Kozeschnik, M. Stockinger, H. Leitner, Adv. Eng. Mater. **12**, 176 (2010)
[6] L. Whitmore, M.R. Ahmadi, L. Guetaz, H. Leitner, E. Povoden-Karadeniz, M. Stockinger, E. Kozeschnik, Mater. Sci. Eng. A **610**, 39 (2014)
[7] M. Kattoura, S.R. Mannava, D. Qian, V.K. Vasudevan, Int. J. Fatigue **104**, 366 (2017)
[8] L.L. Parimi, R.G. A, D. Clark, M.M. Attallah, Mater. Charact. **89**, 102 (2014)
[9] M. Sadowski, L. Ladani, W. Brindley, J. Romano, Addit. Manuf. **11**, 60 (2016)
[10] M. Xia, D. Gu, G. Yu, D. Dai, H. Chen, Q. Shi, Sci. Bull. **61**, 1013 (2016)
[11] P.L. Blackwell, J. Mater. Process. Technol. **170**, 240 (2005)
[12] D. Zhang, W. Niu, X. Cao, Z. Liu, Mater. Sci. Eng. A **644**, 32 (2015)
[13] D. Deng, J. Moverare, R.L. Peng, H. Söderberg, Mater. Sci. Eng. A **693**, 151 (2017)
[14] S. Raghavan, B. Zhang, P. Wang, C.N. Sun, M.L.S. Nai, T. Li, J. Wei, Mater. Manuf. Process. **32**, 1588 (2017)
[15] H. Liu, K. Guo, J. Sun, H. Shi, Mater. Charact. **183**, 111601 (2022)
[16] D. Kong, C. Dong, X. Ni, L. Zhang, C. Man, G. Zhu, J. Yao, J. Yao, L. Wang, X. Cheng, X. Li, J. Alloys Compd. **803**, 637 (2019)
[17] D. Tomus, P.A. Rometsch, M. Heilmaier, X. Wu, Addit. Manuf. **16**, 65 (2017)
[18] M. Ma, Z. Wang, X. Zeng, Mater. Charact. **106**, 420 (2015)
[19] Y.L. Hu, X. Lin, S.Y. Zhang, Y.M. Jiang, X.F. Lu, H.O. Yang, W.D. Huang, J. Alloys Compd. **767**, 330 (2018)
[20] Y.L. Hu, Y.L. Li, S.Y. Zhang, X. Lin, Z.H. Wang, W.D. Huang, Mater. Sci. Eng. A **772**, 138711 (2020)
[21] Y. Zhao, Z. Ma, L. Yu, Y. Liu, Acta Mater. **247**, 118736 (2023)
[22] P. Sun, N. Yan, S. Wei, D. Wang, W. Song, C. Tang, J. Yang, Z. Xu, Q. Hu, X. Zeng, Mater. Sci. Eng. A **868**, 144535 (2023)
[23] W. Zhang, F. Liu, F. Liu, C. Huang, L. Liu, Y. Zheng, X. Lin, J. Mater. Res. Technol. **16**, 1832 (2022)
[24] S. Ghaemifar, H. Mirzadeh, J. Mater. Res. Technol. **24**, 3491 (2023)
[25] Y.N. Zhang, X. Cao, P. Wanjara, M. Medraj, Acta Mater. **61**, 6562 (2013)
[26] M.B. Wilms, S.K. Rittinghaus, M. Goßling, B. Gökce, Prog. Mater. Sci. **133**, 101049 (2023)
[27] F. Yan, W. Xiong, E. Faierson, G.B. Olson, Scr. Mater. **155**, 104 (2018)
[28] H. Yang, L. Meng, S. Luo, Z. Wang, J. Alloys Compd. **828**, 154473 (2020)
[29] X. Zhao, J. Chen, X. Lin, W. Huang, Mater. Sci. Eng. A **478**, 119 (2008)
[30] D. Du, A. Dong, D. Shu, G. Zhu, B. Sun, X. Li, E. Lavernia, Mater. Sci. Eng. A **760**, 469 (2019)
[31] W. Xiao, S. Lu, Y. Wang, J. Shi, Trans. Nonferrous Met. Soc. China **28**, 1958 (2018)
[32] H. Qi, M. Azer, A. Ritter, Metall. Mater. Trans. A **40**, 2410 (2009)
[33] H. Xiao, S. Li, X. Han, J. Mazumder, L. Song, Mater. Des. **122**, 330 (2017)

[34] V.A. Popovich, E.V. Borisov, A.A. Popovich, VSh. Sufiiarov, D.V. Masaylo, L. Alzina, Mater. Des. **131**, 12 (2017)

[35] E. Chauvet, P. Kontis, E.A. Jägle, B. Gault, D. Raabe, C. Tassin, J.J. Blandin, R. Dendievel, B. Vayre, S. Abed, G. Martin, Acta Mater. **142**, 82 (2018)

[36] Y.T. Tang, C. Panwisawas, J.N. Ghoussoub, Y. Gong, J.W.G. Clark, A.A.N. Németh, D.G. McCartney, R.C. Reed, Acta Mater. **202**, 417 (2021)

[37] J.N. DuPont, M.R. Notis, A.R. Marder, C.V. Robino, J.R. Michael, Metall. Mater. Trans. A **29**, 2785 (1998)

[38] J.N. DuPont, A.R. Marder, M.R. Notis, C.V. Robino, Metall. Mater. Trans. A **29**, 2797 (1998)

[39] C. Chu, W. Chen, L. Huang, H. Wang, L. Chen, Z. Fu, Int. J. Plast. **175**, 103939 (2024)

[40] X. Yan, Y. Jiang, Q. Jin, T. Yao, W. Wang, A. Tao, C. Gao, X. Li, C. Chen, H. Ye, X.L. Ma, Nat. Commun. **14**, 2788 (2023)

[41] Z. Zhang, J. Liu, C. Zhu, X. Wang, Y. Zhou, J. Wang, J. Li, Intermetallics **168**, 108272 (2024)

[42] V.A. Vorontsov, J.S. Barnard, K.M. Rahman, H.Y. Yan, P.A. Midgley, D. Dye, Acta Mater. **120**, 14 (2016)

[43] W. Song, X. Wang, J. Li, J. Meng, Y. Yang, J. Liu, J. Liu, Y. Zhou, X. Sun, J. Mater. Sci. Technol. **89**, 16 (2021)

[44] Y. Wu, C. Li, X. Xia, H. Liang, Q. Qi, Y. Liu, J. Mater. Sci. Technol. **67**, 95 (2021)

[45] Q. Gao, Y. Jiang, Z. Liu, H. Zhang, C. Jiang, X. Zhang, H. Li, Mater. Sci. Eng. A **779**, 139139 (2020)

[46] P. Zhang, Y. Yuan, L. Zhong, Y.F. Gu, J.B. Yan, J.T. Lu, Z. Yang, Materialia **16**, 101061 (2021)

[47] Q. Guo, Z. Ma, Z. Qiao, C. Li, T. Zhang, J. Li, C. Liu, Y. Liu, J. Mater. Sci. Technol. **119**, 98 (2022)

[48] X. Zhuang, S. Antonov, L. Li, Q. Feng, Scr. Mater. **202**, 114004 (2021)

[49] L. Tang, J. Liang, C. Cui, J. Li, Y. Zhou, X. Sun, Y. Ding, Mater. Sci. Eng. A **786**, 139438 (2020)

[50] D.M. Stefanescu, R. Ruxanda, ed. by G.F. Vander Voort (ASM International, 2004), pp. 71–92

[51] S. Zhang, L. Wang, X. Lin, H. Yang, W. Huang, Compos. Pt. B Eng. **239**, 109994 (2022)

[52] S. Sui, J. Chen, E. Fan, H. Yang, X. Lin, W. Huang, Mater. Sci. Eng. A **695**, 6 (2017)

[53] E.L. Stevens, J. Toman, A.C. To, M. Chmielus, Mater. Des. **119**, 188 (2017)

[54] W. Song, X.G. Wang, J.G. Li, J. Meng, T.F. Duan, Y.H. Yang, J.L. Liu, J.D. Liu, W.L. Pei, Y.Z. Zhou, X.F. Sun, J. Alloys Compd. **848**, 156584 (2020)